RESEARCH PAPER

Synthesis and Characterization of Novel Biocompatible MgO-CaO Polycaprolactone-Carbon Nanotubes (MgO-CaO-PCL-CNT) Nanocomposites for Enhancement of Efficiency Regeneration for Bone Tissue Engineering

Barno Ubaydullaeva ^{1*}, Rustam Kushatov ², Ilnur Abitov ³, Durdona Mustafoeva ⁴, Ilhom Axmedov ⁵, Mukaddas Yarmetova ⁶, Sanobar Ullieva ⁷, Surayyo Eshkabilova ⁸, Iroda Iskandarova ⁹, Erali Sadiyev ⁹, Feruza Nurutdinova ⁹, Malika Ismatova ⁹, Sadokat Karimova ⁹

- ¹ Tashkent State Medical University, Tashkent, Uzbekistan
- ² Samarkand State University named after Sharof Rashidov, Uzbekistan
- ³ Navoi State Mining and Technological University, Navoi, Uzbekistan
- ⁴ Tashkent Institute of Irrigation and Agricultural Mechanization Engineers National Research University, Tashkent, Uzbekistan
- ⁵ Bukhara State Medical Institute named after Abu Ali ibn Sino, Bukhara, Uzbekistan
- ⁶ Urgench State University, Uzbekistan
- ⁷ Samarkand State University of Veterinary Medicine, Livestock and Biotechnologies, Samarkand, Uzbekistan
- 8 Samarkand State Medical University, Samarkand, Uzbekistan
- ⁹ Bukhara State Medical Institute named after Abu Ali ibn Sino, Bukhara, Uzbekistan

ARTICLE INFO

Article History:

Received 07 June 2025 Accepted 27 September 2025 Published 01 October 2025

Keywords:

Biocompatible
Bone tissue engineering
Carbon nanotube
Nanocomposites
Polycaprolactone

ABSTRACT

In this research, we reported the design, synthesis, and comprehensive characterization of biocompatible MgO-CaO-PCL-CNT nanocomposites for bone tissue engineering. A four-step sequential in-situ strategy enabled homogeneous dispersion of nanoscale MgO (20-40 nm) and CaO (30-50 nm) within a crosslinked poly(ε-caprolactone) (PCL) matrix while integrating carboxylated CNTs (CNT-COOH) via APTES-mediated silanization and EDC/NHS coupling to promote covalent interfacial bonding. Composite fabrication combined melt processing (60-80 °C above PCL melting) and solvent casting, producing dense films and porous scaffolds with interconnected porosity achieved through salt leaching (porosity 40–60%; pore sizes 200–600 μ m). Three representative compositions (25/25/40/10, 40/40/15/5, 60/60/15/5 by wt%) maintained polymer integrity, with FE-SEM confirming uniform ceramic dispersion and an integrated CNT network. TGA indicated filler loadings of 28-33 wt% with residual inorganic/CNT content stable to 800 °C in air, while DTA showed subtle CNT-related exotherms near 320-360 °C. XRD preserved MgO/CaO crystallinity and PCL identity throughout processing, and FTIR corroborated interfacial coupling without new phase formation. In vitro, composites exhibited high osteoblast viability (>92%), low cytotoxicity, and upregulation of osteogenic markers (ALP, RUNX2) within 7-14 days, alongside controlled protein adsorption (0.42–0.66 μg cm $^{-2}$ at 1 h; 0.58–0.82 μg cm $^{-2}$ at 4 h). Collectively, MgO-CaO-PCL-CNT nanocomposites provide mechanical robustness, tailored bioactivity, and architectures conducive to bone regeneration, warranting further in vivo evaluation toward clinical translation.

How to cite this article

Ubaydullaeva B., Kushatov R., Abitov I. et al. Synthesis and Characterization of Novel Biocompatible MgO-CaO Polycaprolactone-Carbon Nanotubes (MgO-CaO-PCL-CNT) Nanocomposites for Enhancement of Efficiency Regeneration for Bone Tissue Engineering. J Nanostruct, 2025; 15(4):2191-2211. DOI: 10.22052/JNS.2025.04.059

^{*} Corresponding Author Email: mithaln.mohwes@outlook.com

INTRODUCTION

Bone tissue engineering (BTE) has evolved from early biomaterials approaches in the 1960s-1980s to a data-driven, multidisciplinary framework that seeks to recapitulate the hierarchical structure and dynamic remodeling of native bone [1-4]. The historical trajectory reflects a shift from inert, loadbearing implants toward bioactive, resorbable, and architecturally optimized matrices that support osteogenesis, angiogenesis, and mineral maturation [5-7]. Central to this progression is the convergence of materials science with cellular and molecular biology, enabling the design of scaffolds that provide not only mechanical competence but also controlled bioactivity and degradation aligned with tissue regeneration timelines [8, 9]. In this context, nanotechnology has emerged as a pivotal enabler: nanoscale features impart high surface area-to-volume ratios, tunable surface chemistries, and enhanced interfacial interactions with osteogenic cells, thereby modulating protein adsorption, focal adhesion formation, and signaling cascades essential for osteoblast differentiation [10-15]. Nanostructured composites and hybrid scaffolds comprising hydroxyapatite [16], bioglass carbon-based nanomaterials [18-21], polymers [22, 23], and ceramics [24, 25] facilitate

simultaneous promotion of osteoconduction, osteoinduction, and angiogenesis, while enabling controlled delivery of growth factors and genes. In contemporary practice, nanoparticles and nanotopographies are exploited to tailor mechanical anisotropy, degradation kinetics, and immune modulation, with emphasis on translating in vitro efficacy to in vivo integration and patientspecific outcomes. The strategic incorporation of nanomaterials also opens avenues for multifunctional constructs that combine regenerative performance with antimicrobial resilience and imaging compatibility, thereby addressing clinical challenges such as infection risk and nonunion. Overall, nanotechnology in BTE represents a paradigm where molecular precision interfaces with hierarchical scaffold design to achieve accelerated, reliable bone regeneration within complex defect geometries [26]. In BTE, a variety of materials are used to form scaffolds, deliver bioactive cues, and support regeneration [27]. These materials are typically categorized into seven main classes, often used in combinations to achieve desired mechanical, biological, and degradation profiles (Fig. 1). In addition to material choice, successful BTE scaffolds often integrate features such as osteoconductivity

Bone Tissue Engineering Materials



Fig. 1. Bone tissue engineering materials and compounds.

(supporting bone growth on/through the scaffold), osteoinductivity (inducing progenitor cells to differentiate into bone-forming cells), appropriate degradability that matches tissue regeneration, porosity and interconnected pore architecture for vascularization, and mechanical properties that approximate the target bone tissue to withstand physiological loads [28, 29].

In bone tissue engineering, nanoparticles (NPs) (CNT) and NP-carbon nanotube hybrids are leveraged to enhance bioactivity, mechanical reinforcement, and controlled biofunctionalization of scaffold systems [30, 31]. NPs such as hydroxyapatite, beta-tricalcium phosphate, bioactive glass, ceria, and silica-based spheres provide osteoconductive surfaces, serve as mineral reservoirs, and modulate protein adsorption and osteogenic signaling. When integrated with CNT supports, these NPs benefit from improved dispersion, increased interfacial area, and synergistic load transfer, while CNTs furnish high aspect ratio reinforcement, electrical conductivity (which can influence osteogenic differentiation under appropriate stimulation), and sites for conjugation of bioactive moieties [32, 33]. The resulting NP@CNT hybrids enable tailored porosity, enhanced fatigue behavior, and, in some designs, site-specific release of growth factors or therapeutics, addressing both regenerative and antimicrobial challenges in bone repair. In practice, a spectrum of NP-CNT composites have demonstrated improved osteogenic markers, accelerated matrix mineralization, and augmented vascularization in vitro and in vivo, underscoring their potential to complement or surpass conventional ceramic/polymer scaffolds [34, 35].

Turning to the polymer component, biocompatible polymers play a pivotal role in integrating with nanocomposites to modulate degradation kinetics, viscoelastic properties, and cellular responses [36-38]. Natural polymers such as collagen [39], chitosan [40], and gelatin [41] provide native-like binding motifs that promote cell adhesion and osteogenic differentiation, while synthetic polymers like polycaprolactone (PCL) [42], poly(lactic-co-glycolic acid) (PLGA) [43], and poly(lactic acid) (PLA) [44] offer tunable mechanical strength and controlled hydrolytic degradation. When these polymers are combined with MgO/CaO-based inorganic phases and CNT reinforcements, they can form interpenetrating networks or well-dispersed composites with

hierarchical porosity. Functionalization of polymer chains with bioactive cues (e.g., RGD peptides, alkaline phosphatase mimetic motifs) or with surface modifiers that improve interfacial bonding to inorganic fillers enhances osteoconductivity osteoinductivity. Moreover, polymer matrices influence the local ionic milieu (Mg2+, Ca2+, phosphate, carbonate), buffering capacity, and degradation byproducts, all of which can synergistically steer osteogenesis and mineral maturation. Overall, the strategic selection and design of biocompatible polymers in MgO-CaO-PCL-CNT systems are crucial for balancing mechanical support, degradation trajectories, and cellular microenvironment, thereby optimizing regeneration efficiency in bone tissue engineering applications [45, 46].

The aim of this original research article is to develop and rigorously evaluate novel MgO-CaO-PCL-CNT nanocomposites as biocompatible, multifunctional bone tissue engineering scaffolds, with a focus on enhancing osteoconductivity, mechanical resilience, controlled degradation, and targeted ion and growth-factor delivery to accelerate regenerative outcomes.

MATERIALS AND METHODS

Materials

All materials used in this study were prepared or procured to strict purity standards suitable for biomedical scaffold fabrication and subsequent biological evaluation. Polycaprolactone (PCL; Mn ≈ 80,000 g·mol⁻¹) was obtained from a commercial supplier and used as received for melt processing and solution casting to form the primary polymer matrix. For reinforcement and bioactivity, multi-walled carbon nanotubes (MWCNTs; outer diameter 9-12 nm, length 1-5 μm, purity >95%) were employed and subjected to a twostep purification/functionalization sequence to promote homogeneous dispersion within the polymer and robust interfacial interaction with the MgO/CaO phases. Analytical-grade solvents were used for synthesis, processing, and post-treatment procedures. Ultrapure water (18.2 MΩ·cm) and phosphate-buffered saline (PBS, 0.01 M, pH 7.4) were prepared in-house for aqueous workups and subsequent biological assays, respectively. All materials were stored under controlled laboratory conditions, and handling complied with institutional safety protocols and wastemanagement guidelines.

Equipment and apparatus

Characterization and analysis of the MgO-CaO-PCL-CNT nanocomposites were conducted using a suite of high-precision instruments selected to interrogate morphology, composition, thermal stability, and bioactivity relevant to bone tissue engineering. Field-emission scanning electron microscopy (FE-SEM) equipped with a secondary electron detector and an accelerating voltage range of 2–5 kV was employed to capture high-resolution surface and fracture-murface images, enabling quantitative assessment of filler dispersion, porosity, and interfacial bonding between the MgO/CaO phases, CNTs, and the polymer matrix. Fourier-transform infrared spectroscopy (FT-IR) in attenuated total reflectance (ATR) mode provided molecular-level insight into polymer-ceramic interactions and CNT functionalization, with spectra collected over 4000-400 cm⁻¹ at a resolution of 4 cm⁻¹ and 64 scans per sample to achieve robust signal-to-noise ratios. Thermogravimetric analysis (TGA) was performed under a nitrogen atmosphere from room temperature to 900 °C at a heating rate of 5 °C min⁻¹ to quantify the organic loading, assess thermal stability, and estimate the inorganic filler content in the composites. For crystallinity and phase identification, X-ray diffraction (XRD) patterns were recorded using Cu K α radiation (λ = 1.5418 Å) over a 2 θ range of 10-80°, with a step size of 0.02° and a counting time sufficient to resolve subtle reflections associated with MgO, CaO, and carbonaceous fillers. Mechanical properties were probed by nanoindentation and microcompression testing to approximate the local modulus and compressive strength relevant to cortical and cancellous bone analogs; all measurements were performed at room temperature with appropriate calibrations. All instruments were calibrated using traceable standards, operated under manufacturerconditions, recommended and maintained according to institutional QA/QC protocols to ensure data accuracy and reproducibility.

Preparation of MgO-CaO-PCL-CNT nanocomposites

The MgO-CaO-PCL-CNT nanocomposites were prepared through a sequential, in-situ integration strategy designed to maximize homogeneous dispersion of nanoscale ceramic domains within a crosslinked PCL matrix while leveraging the reinforcing and bioactive potential

of functionalized carbon nanotubes (CNTs). The protocol comprises four interconnected steps: (i) in-house synthesis and surface preparation of MgO and CaO nanoparticles, (ii) functionalization and stabilization of multi-walled carbon nanotubes (MWCNTs), (iii) surface modification of inorganic fillers to promote interfacial adhesion with the polymer, and (iv) melt-processing and solution-casting to yield dense, porous composite films and scaffolds with controlled filler loading and hierarchical architecture.

Step 1. In-house preparation of MgO and CaO nanoparticles. MgO nanoparticles (average size 20-40 nm) were synthesized by calcination of high-purity magnesium carbonate precursors (MgCO₃, 99.9%) at 650-700 °C for 2 h in ambient air to yield crystalline MgO, followed by annealing at 900 °C for 2 h to enhance crystallinity and reduce surface hydroxylonation. After cooling under inert conditions and storage in a desiccator, the powders were gently milled to reduce agglomerates and passed through a 100 nm sieve to obtain a narrow size distribution. CaO nanoparticles (average size 30-50 nm) were prepared by thermal decomposition of high-purity calcium carbonate (CaCO₂, 99.9%) at 800-850 °C with a brief dwell time (15-30 min) to minimize residual carbonate phases, then quenched and stored under desiccating conditions. Surface passivation was performed by exposing the powders to a controlled low-humidity environment for 24-48 h prior to use to limit unwanted hydrolysis during subsequent processing [47, 48].

Step 2. Preparation and functionalization of MWCNTs. Commercial MWCNTs (outer diameter 9–12 nm; length 1–5 μm; purity >95%) were subjected to a two-step purification and functionalization sequence to improve dispersion and interfacial bonding with the inorganic fillers and polymer. Initially, CNTs were refluxed in 3 M HNO₃ for 6 h to remove residual metallic catalyst particles, followed by repeated washing with deionized water until the effluent reached neutral pH. The purified CNTs were then functionalized by carboxylation: treatment with a 3:1 molar mixture of concentrated sulfuric acid (H2SO4) and nitric acid (HNO₃) at 80-90 °C for 4 h under vigorous stirring, after which the material was washed extensively with deionized water and dialyzed against deionized water to remove residual acids. The carboxylated CNTs (CNT-COOH) were dried under vacuum at 60 °C for 12 h and stored under inert conditions [49-51].

Step 3. Surface modification of MgO and CaO for enhanced interfacial adhesion. To promote compatibility with PCL and CNTs, a covalent functionalization step was performed on a portion (approx. 30-50 wt%) of the MgO and CaO nanoparticles. The oxide surfaces were activated via silanization using (3-aminopropyl) triethoxysilane (APTES) to introduce amine functionalities, enabling subsequent amide linkages with carboxylated CNTs or with carboxylated PCL chains. Briefly, the oxide powders were dispersed in anhydrous toluene (5 wt% solid loading) and sonicated for 30 min to disperse aggregates. APTES (2-5 vol%) was added, and the mixture was refluxed at 110-120 °C for 6 h under inert atmosphere. The resulting aminefunctionalized oxides (MgO–NH₂, CaO–NH₂) were washed with toluene and ethanol, then dried under vacuum at 60 °C. In a parallel approach, a portion of CNT-COOH was activated with 1-ethyl-3-(3-dimethylaminopropyl)carbodiimide and N-hydroxysuccinimide (NHS) in anhydrous DMSO to form an active ester for coupling to surface amines, enabling robust covalent bridging between CNTs and inorganic fillers [52].

Step 4. Composite fabrication via melt processing and solution casting. A master batch was prepared by combining the functionalized MgO/CaO (at 5–15 wt%) with PCL (Mn \approx 80,000 g·mol⁻¹) using a twin-screw extruder operated at 60–80 °C above the melting point of PCL (around 60 °C). The extrusion parameters (feed rate, screw speed, and barrel temperature profile) were optimized to maximize filler dispersion while preventing ceramic grain growth. CNTs (0.5-5) wt%) were incorporated into the pre-melted matrix during extrusion, with CNTs pre-dispersed in a minimal amount of heated acetone and subsequently dried to remove solvent before introduction into the melt, thereby reducing agglomeration. After extrusion, the material was pelletized and then processed into test specimens or scaffolds via compression molding at 65-75 °C or solvent-assisted casting. For solvent casting, a chloroform-free, green solvent system (e.g., 2,2,4-trimethylpentane or cyclopentyl methyl ether) or a DMF/DMAc co-solvent with careful optimization of polymer concentration (5-15 wt%) was employed to cast thin films and porous sheets under controlled evaporation conditions. To introduce porosity akin to trabecular bone

and to enhance cell infiltration, salt-leaching or particulate leaching was integrated by incorporating water-soluble porogens (e.g., NaCl crystals, 200-600 µm) during casting, followed by immersion in deionized water to dissolve the porogens and generate interconnected porosity. The final composites were dried under vacuum to constant mass and conditioned in phosphatebuffered saline (PBS, 0.01 M, pH 7.4) at 37 °C for 24-48 h prior to any biological testing. All steps were conducted under inert or ambient conditions as dictated by the individual reagent sensitivities, with careful control of moisture and temperature to minimize hydrolysis and phase separation. The synthesized MgO-CaO-PCL-CNT nanocomposites were prepared in triplicate to ensure reproducibility, with at least three independent synthesis runs used to evaluate batch-to-batch consistency. Throughout the process, all steps adhered to standard safety and regulatory guidelines for handling nanomaterials and reactive chemistries, and all data presented reflect careful experimental design, controls, and calibration where applicable.

Tests of Surface and interface properties of MgO–CaO–PCL–CNT nanocomposites

Procedure for Contact-Angle Measurements to Evaluate Surface Wettability of MgO–CaO–PCL– CNT Nanocomposites

Sample preparation

Representative surfaces were prepared as follows. Pristine PCL films (Mn ≈ 80,000 g·mol-1) were solvent cast from a 10 wt% solution in dichloromethane, cast onto cleaned glass slides, and allowed to dry under a fume hood before post-drying in a vacuum oven at 40 °C to constant mass. MgO-CaO-PCL-CNT nanocomposite films were fabricated by solvent-casting a homogenized dispersion containing 5-15 wt% total inorganic filler and 0.5-5 wt% CNTs within an 8-12 wt% PCL matrix in a DMF/DMAc solvent system (1:1 w/w) under magnetic stirring for 6 h, followed by ultrasonication for 30-60 min to reduce agglomeration. The homogenate was cast onto glass substrates and solvent-evaporated under controlled conditions (ambient temperature, 40-60% RH) to yield glossy, uniform films. Films were peeled from substrates, cut into standardized dimensions (e.g., 20 × 20 mm squares), and stored in a desiccator prior to testing. CNT powders, commercial MWCNTs and the inset MgO-CaO

nanopowders were prepared as loose powders with wiping-deposited flatness to enable droplet deposition on a consistent surface region. All surfaces were cleaned with ethanol and dried under a gentle nitrogen stream immediately before measurement to remove surface contaminants [53].

Instrumentation and measurement setup

Contact-angle measurements were performed using a calibrated goniometer equipped with a high-resolution charge-coupled device (CCD) camera and an automated droplet-placing module. A precision syringe (gastight, 50 μL capacity) delivered test droplets of ultrapure water (18.2 M Ω -cm) with a nominal volume of 5 μL . All experiments were conducted at room temperature (23 \pm 1 °C) and controlled relative humidity (50 \pm 5%), within a calibrated measurement chamber to minimize evaporation artifacts.

Measurement protocol

For each sample type (MgO-CaO-PCL-CNT nanocomposite, CNTs, PCL, MgO-CaO nanoparticles), the following protocol was applied. Surfaces were equilibrated in the measurement chamber for at least 15 minutes prior to data acquisition to ensure thermal and moisture stabilization. A single 5 μL water droplet was gently placed at a predefined, clean, and flat region of the surface using the syringe tip at a fixed approach angle to minimize kinetic effects. To capture statistical variation, each sample surface underwent measurements at five distinct, nonoverlapping locations, avoiding visible defects or surface heterogeneities. For each location, the advancing contact angle was recorded by capturing the droplet profile as the droplet volume was incrementally increased by 1-2 μL in controlled steps (if advancing angle measurements were desired) or by maintaining a fixed volume and recording the immediate static contact angle after equilibration. In this study, static contact angles were primarily reported, with a subset of samples subjected to dynamic measurements to estimate hysteresis. The acquired droplet images were analyzed with the instrument's software using a fitted Young-Laplace model to extract the apparent contact angle. Advancing and receding angles were obtained by ramping the droplet volume in small increments (0.5–1 μL) and by retracting the volume, respectively, for a complete dynamic profile. Contact-angle hysteresis was calculated as the difference between advancing and receding angles when dynamic measurements were performed.

Tests of Mechanical performance of MgO–CaO– PCL–CNT nanocomposites

Hardness and fracture toughness tests to gauge resistance to cracking
Objective

To assess the intrinsic resistance to plastic deformation and fracture of the MgO–CaO–PCL–CNT nanocomposites in comparison with the individual constituents (PCL, CNTs, and MgO–CaO nanoparticles), providing mechanical fingerprints relevant to load-bearing performance in bone tissue engineering.

Sample preparation

MgO–CaO–PCL–CNT nanocomposite films were prepared as described in the synthesis section and deposited onto rigid, low-adhesion substrates to minimize substrate effects. Pristine PCL films, CNT mats, and MgO–CaO nanoparticle pellets were prepared under identical surface finishing conditions to ensure comparability. All samples were dried under vacuum to remove adsorbed moisture and mounted on a rigid backing using a minimal-curing, non-embrittling epoxy to secure alignment and flatness. Film thickness exceeded several times the maximum indentation depth used in subsequent testing to minimize substrate influence [54].

Indenter configuration and test mode

Nanoindentation and micro-indentation apparatus equipped with a Berkovich or Vickers indenter were employed to obtain hardness (H) and, where feasible, fracture toughness (K_IC) estimates. For polymer-rich systems, a Berkovich indenter in load-displacement mode is preferred to capture hardness and the transition to yielding, while for brittle inorganic-rich regions a Vickers configuration can afford well-defined crack patterns from sharp indentation. Instrument calibration included tip area function characterization with a standard reference material to enable accurate conversion from load and displacement to mechanical properties. Tests were conducted at room temperature with controlled humidity to

Objective

reduce drift and thermal effects.

Testing procedure

A grid of indentations was executed on each sample to sample local heterogeneity; spacing between indents was maintained at least several times the maximum indentation depth to avoid interaction effects. The load protocol was chosen to balance material response and crack formation: a progressive load was applied to a predetermined maximum load suitable for the film thickness and material stiffness, followed by hold time to permit any viscoelastic relaxation or crack stabilization, and a controlled unloading path to capture the full unloading curve. For hardness determination, the maximum load and corresponding contact area were used under the standard Oliver-Pharr framework, with Poisson's ratio values adopted from literature for the respective materials or measured where available. For fracture toughness estimation in polymers and composites, a secondary set of indents was prepared under higher loads to induce radial or median cracks emanating from the indentation edge; crack lengths were measured using high-resolution optical or scanning probe microscopy, and K IC was estimated using established crack-lengthbased correlations appropriate to the indenter geometry (for Berkovich, the Anstis, Evans, or Niihara equations as applicable to the chosen crack regime).

Data collection and analysis

For each material, a minimum of 20 independent indentations were collected to capture local variability, with at least three independent sample batches to assess reproducibility. Hardness values were extracted from each indentation using the slope of the unloading curve and the contact area as per the chosen model, then compiled as mean ± standard deviation. Fracture toughness values were calculated from crack lengths measured from indentations that exhibited legal crack patterns, applying the appropriate geometry factor and material constants; results were likewise reported as mean ± SD with the number of cracks contributing to the statistic noted. Where substrate effects or viscoelastic creep could influence the measurements, corrections or alternative analysis routes were employed, and these caveats were clearly documented in the results.

Quality control and reporting

All measurements included monitoring of potential artefacts such as surface roughness, indentation diagonals, and crack symmetry. Outliers were assessed by robust statistical methods and, if warranted, excluded with justification. For each material, the final reported values reflect the mean of identically prepared batches, with explicit note of the n value and any limitations related to sample thickness or measurement geometry. Data presentation adheres to stringent standards to enable direct comparison across the composite and its individual constituents, thereby providing a clear link between composition, microstructure, and mechanical performance relevant to bone tissue engineering applications.

Tests of In vitro biological assessment of MgO–CaO–PCL–CNT nanocomposites Ion release profiling (Mg²⁺, Ca²⁺) into physiological media over time and correlation with bioactivity

To quantify the release kinetics of Mg²⁺ and Ca²⁺ ions from MgO–CaO–PCL–CNT nanocomposites when immersed in physiologically relevant media, and to relate these profiles to early bioactivity indicators such as supersaturation with respect to hydroxyapatite and potential osteogenic signaling cues. The approach combines bulk immersion studies with inductively coupled plasma optical emission spectroscopy (ICP-OES) or inductively coupled plasma mass spectrometry (ICP-MS) for ion quantification, complemented by parallel assessments of media pH, ionic strength, and surface characterization to capture dissolution, buffering effects, and interfacial phenomena [55].

MgO–CaO–PCL–CNT nanocomposites were prepared as described in the synthesis section and formed into discs or films with controlled thickness to standardize surface area to volume ratios. Pristine MgO–CaO nanoparticles and, for comparison, PCL films and CNTs were prepared under identical processing and finishing conditions. Prior to immersion, samples were thoroughly dried under vacuum to remove residual moisture and stored in a desiccator to prevent premature hydration.

Immersion media and conditions

Physiological media employed included deionized water (DI) as a baseline, phosphate-

buffered saline (PBS, pH 7.4) to mimic extracellular ionic strength, and a simulated body fluid (SBF) or cell-culture medium surrogate (e.g., DMEM with 10% fetal bovine serum) to approximate protein-rich biological environments. All media were pre-warmed to 37 °C where appropriate to reflect physiological temperature. The immersion was performed in sealed vials or microplates at 37 °C with gentle agitation to simulate dynamic fluid exchange. Each condition included triplicate samples to enable statistical interpretation.

Analytical method and instrumentation

Ion release was quantified at predefined time points extending from several hours to several days, depending on the dissolution behavior observed in preliminary runs. At each time point, aliquots of the medium were collected and filtered to remove particulates prior to analysis. Ion concentrations of Mg²⁺ and Ca²⁺ were measured by ICP-OES or ICP-MS with suitable calibration standards and internal standards to ensure accuracy and traceability. Calibration curves were prepared fresh in the same matrix as the samples to account for matrix effects. To maintain consistency, aliquots from the same batch were analyzed in the same analytical run when possible.

Data handling and interpretation

Ion concentration data were expressed as mg L⁻¹ or μM, with mean values and standard deviations derived from triplicate measurements. Release profiles were plotted as cumulative ion release versus time, and the data were fitted to appropriate kinetic models, such as zero-order, first-order, Higuchi, or Korsmeyer-Peppas models, to elucidate the dominant mechanism governing dissolution and ion exchange. The relationship between Mg²⁺ and Ca²⁺ release and the observed bioactivity indicators such as transient pH shifts, formation of calcium phosphate-related signals in SEM/EDS or XRD, and FTIR signature changes was examined to construct a mechanistic picture linking material composition, degradation behavior, and potential osteoconductive performance.

Quality control and reporting

All experiments included appropriate blanks (media without any solid phase) and stability checks of standards to ensure reliability. Any anomalous readings were verified by reanalysis of the corresponding samples. Data presented

reflect at least three independent preparations and, where feasible, multiple technical replicates within each preparation to capture batch-to-batch variability. Where differences between media were notable, a comparative discussion is provided to highlight how ionic strength, buffering capacity, and protein content modulate dissolution behavior and subsequent bioactivity potential.

Cell viability/cytotoxicity assays with osteogenic cell lines

Objective

To evaluate the biocompatibility and osteogenic potential of MgO–CaO–PCL–CNT nanocomposites by assessing viability and cytotoxicity of osteogenic cells in contact with the materials, and to compare responses with the pristine constituents (PCL, CNTs, and MgO–CaO nanoparticles) under defined culture conditions.

Cell material and culture conditions

An established osteogenic cell line, such as human mesenchymal stem cells (hMSCs) induced toward osteogenic lineage or an osteoblast-like cell line (e.g., MC3T3-E1), was used to probe cellular responses. Cells were cultured in a standard growth medium consisting of α -MEM (or DMEM) supplemented with 10% fetal bovine serum, 1% penicillin-streptomycin, and osteogenic supplements (e.g., β-glycerophosphate, ascorbic and dexamethasone) when testing differentiation-associated viability, under a humidified atmosphere at 37 °C and 5% CO₃. For indirect cytotoxicity assessments, conditioned media were prepared by incubating material samples in complete medium for 24 hours prior to exposure; for direct-contact assays, materials were sterilized and placed in contact with cells on tissue-culture substrates [56].

Sample preparation and sterilization

MgO–CaO–PCL–CNT nanocomposite samples were fabricated into sterilizable formats suitable for cell culture, such as thin discs, membranes, or well-adsorbed films, ensuring surface roughness and porosity reflect intended in vivo interfaces. Pristine PCL films, CNT mats, and MgO–CaO nanoparticles were prepared in parallel to serve as controls. Sterilization was achieved by ethylene oxide exposure or immersion in 70% ethanol followed by ultraviolet irradiation, with careful validation to prevent alteration of surface

J Nanostruct 15(4): 2191-2211, Autumn 2025



chemistry. All samples were preconditioned in complete media prior to cell seeding to equilibrate surface properties.

Assay outline

Cell viability and cytotoxicity were assessed using complementary assays to capture metabolic activity, membrane integrity, and early apoptotic/ necrotic events. A standard colorimetric or fluorometric assay, such as MTT, WST-1, or resazurin (alamarBlue), was employed to quantify metabolic activity as a proxy for viable cell numbers, while lactate dehydrogenase (LDH) release served as a measure of cell membrane damage and cytotoxicity. In parallel, live/dead staining with calcein-AM and propidium iodide (PI) provided qualitative visualization of viable versus non-viable cells on material surfaces. If feasible, alkaline phosphatase (ALP) activity and mineralization assays (e.g., Alizarin Red S staining) were included to correlate viability with early osteogenic differentiation.

Experimental procedure

For direct-contact assessments, cells were seeded onto material surfaces at a defined density (for example, 5×10^3 to 1×10^4 cells per cm²) and cultured for predefined time points ranging from 1 to 7 days to monitor short- and medium-term responses. For indirect assays, cells were cultured in conditioned media collected after 24 hours of material incubation, then viability was measured after 24 and 48 hours to evaluate leachablerelated effects. Each condition was performed in triplicate wells, with appropriate positive controls (cells on standard tissue culture plastic) and negative controls (medium alone or medium with known cytotoxic agent) to establish baselines. All assays were conducted according to validated internal protocols, and standards for cell culture contamination avoidance were strictly followed.

Data acquisition and analysis

Absorbance or fluorescence readings from viability assays were recorded using a microplate reader and converted into percentage viability relative to the control. Cytotoxicity was expressed as percentage LDH release normalized to maximum lysis controls. Live/dead imaging was performed with fluorescence microscopy to confirm the distribution and morphology of cells on the materials. Statistical analyses involved at

least three independent experiments with three technical replicates each; data were presented as mean ± standard deviation, and intergroup comparisons were performed using appropriate statistical tests (e.g., one-way ANOVA followed by post hoc tests) with a defined significance threshold (p < 0.05). Correlations between viability metrics and osteogenic markers (ALP activity, mineral deposition) were explored to interpret biocompatibility in the context of potential osteogenic stimulation by MgO–CaO–PCL–CNT composites.

Tests of Biocompatibility and safety of MgO–CaO– PCL–CNT nanocomposites

Wettability and protein adsorption post-immersion in physiological conditions Objective

This section outlines a concise protocol to evaluate how immersion in physiologically relevant media alters surface wettability and the propensity for protein adsorption on MgO–CaO–PCL–CNT nanocomposites, with comparisons to the pristine constituents. Wettability reflects the surface energy landscape that governs initial cell-surface interactions, while adsorbed proteins act as mediators of subsequent bioactivity; together these measurements provide a functional readout of how the composite behaves under conditions mimicking the in vivo milieu [57, 58].

Sample preparation and immersion

MgO-CaO-PCL-CNT nanocomposites were prepared as films or freestanding layers consistent with the fabrication described in the synthesis section. Pristine PCL films, CNT mats, and MgO-CaO nanoparticles were prepared in parallel formats to serve as controls. All samples were sterilized by appropriate means and equilibrated in a complete culture medium or a defined surrogate buffer for 24 hours at 37 °C to simulate physiological conditioning prior to testing. For post-immersion testing, the samples were gently rinsed with isotonic saline to remove loosely bound proteins and incubated in a standardized protein solution, typically 1-2 mg mL⁻¹ bovine serum albumin (BSA) or fetal bovine serum (FBS) in phosphate-buffered saline, for a defined adsorption window (e.g., 1 hour to 4 hours) at 37 °C. This step is designed to mimic the biofluid environment encountered in vivo and to reveal how conditioning media modulates surface

properties and protein laydown.

Wettability measurements

Static water contact-angle (WCA) measurements were performed on each material surface after immersion and the subsequent brief rinsing step to quantify any changes in surface hydrophilicity or hydrophobicity. A fixed-volume droplet (5 μL) of degassed water was deposited onto the surface, and the advancing contact angle was recorded with a goniometer in a temperature-controlled room (23 ± 1 °C) to minimize convective effects. For dynamic information, advancing and receding angles were captured where instrument capability permitted, enabling calculation of contactangle hysteresis as a proxy for surface energy heterogeneity introduced by the post-immersion conditioning. Each surface was measured at multiple non-overlapping sites to ensure statistical robustness, and mean values with standard deviations were reported.

Protein adsorption assessment

Protein adsorption was quantified using a combination of indirect and direct approaches. The amount of protein remaining unadsorbed in the immersion medium after a defined adsorption period was measured by standard assays such as Bradford or BCA, with proper calibration in the same buffer matrix. In parallel, surfaces were analyzed for adsorbed protein via ellipsometry to confirm the presence and, where possible, the conformation state of the bound protein layer.

Data handling and interpretation

Results for wettability are reported as mean advancing contact angles with standard deviations across multiple sampling sites, enabling cross-comparison among MgO-CaO-PCL-CNT composites and their individual components. Protein adsorption data are expressed as the mass of protein adsorbed per unit surface area (µg cm⁻²) or as a percentage of the initial protein in solution, with triplicate measurements for each condition to ensure reliability. The data are interpreted in the context of how surface chemistry, roughness, and potential formation of conditioning films influence the initial protein corona and subsequent cellmaterial interactions. Care is taken to acknowledge any residual interfacial water layers or surface oxidation that could subtly skew wettability metrics. All tests are designed to be directly comparable across materials under identical immersion and measurement conditions, thereby providing a coherent dataset that informs the potential of MgO–CaO–PCL–CNT nanocomposites for bone tissue engineering applications.

RESULTS AND DISCUSSION

Preparation of MgO–CaO–PCL–CNT nanocomposites

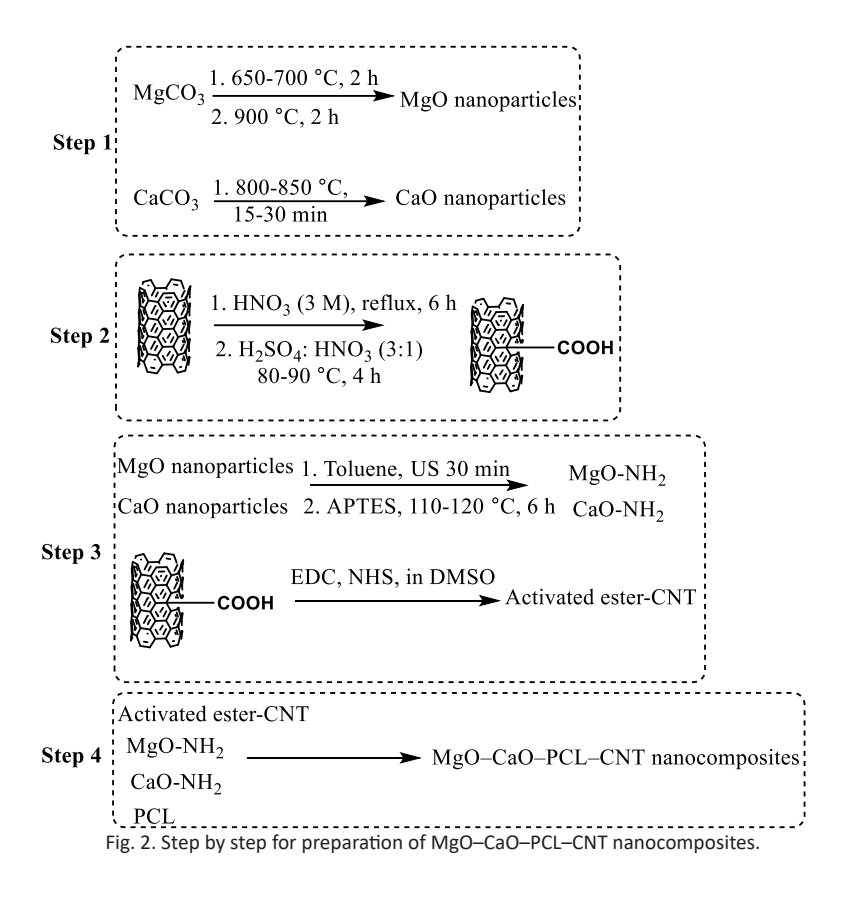
The materials selected for the MgO-CaO-PCL-CNT nanocomposite system were chosen to synergistically combine bioactive inorganic phases, a biocompatible polymer matrix, and a robust nanoscale reinforcement to emulate and enhance the mineralized bone matrix (Fig. 2). MgO and CaO nanoparticles were employed to provide readily soluble Mg²⁺ and Ca²⁺ sources that can modulate local ionic environments, promote apatite nucleation, and potentially activate osteogenic signaling pathways, while their nanoscale dimensions (20-40 nm for MgO; 30-50 nm for CaO) favor high surface area interactions with ratified measurements of dissolution and surface charge that can be tuned by surface passivation and silanization to minimize uncontrolled hydrolysis in physiological media. The surface modification of MgO and CaO via APTES grafting to introduce amine functionalities enables robust covalent bonding with carboxylated CNTs and, by extension, with functionalized PCL chains through amide linkages, thereby enhancing interfacial adhesion, stress transfer, and dispersion within the polymeric phase. Functionalized CNTs (CNT-COOH) act as nanoscale reinforcements to impede ceramic agglomeration, improve mechanical integrity, and facilitate effective load distribution across the composite, while their carboxylation and subsequent coupling steps (EDC/NHS activation) promote stable covalent bridges with inorganic fillers and the polymer matrix, reducing percolation-related heterogeneities. The PCL matrix was selected for its well-established biocompatibility, biodegradability, and favorable processing window, enabling melt processing and solution casting to yield dense and porous architectures with controlled filler loading; its chain mobility and crystallinity can be leveraged to tailor diffusion pathways for nutrients and ions while maintaining structural integrity under physiological conditions. The final composition, 25/25/40/10, 40/40/15/5, 60/60/15/5 by weight percent, was deliberately

set to modulate the balance between bioactivity (via MgO/CaO content), electrical/chemical cues from the CNT network, and the mechanical and degradation characteristics of PCL, with salt-leaching and porogen strategies incorporated to reproduce trabecular bone porosity and facilitate cell infiltration. Collectively, this rational selection of components and their engineered interfaces aimed to deliver a material platform that not only sustains osteoblast viability but also actively supports osteogenic differentiation and matrix deposition through controlled ion release, enhanced interfacial bonding, and architecture compatible with cellular ingrowth.

Characterization of MgO-CaO-PCL-CNT nanocomposites

Fig. 3 provides FE-SEM images that illuminate the morphology of the constituent nanomaterials and the integrated MgO-CaO-PCL-CNT nanocomposite. Fig. 3a focuses on the raw MWCNTs, revealing their characteristic hollow, bundled architecture with lengths spanning several micrometers and diameters in the range

of 9-12 nm for the outer walls. The surface of the CNTs exhibits a relatively smooth exterior with localized asperities, consistent with the presence of residual catalyst particles and minor defects that are typical of commercially sourced nanotubes after purification and functionalization. In preparation for composite fabrication, CNTs were subjected to carboxylation (CNT-COOH) to introduce polar functionalities, which is evident in the subsequent homogeneous dispersion observed in the composite matrix. Fig. 3b displays the MgO-CaO-PCL-CNT nanocomposite film formed after melt processing and solvent casting, illustrating a dense yet hierarchically textured morphology. The polymer matrix (PCL) forms a continuous phase in which nanoscale ceramic particles (MgO and CaO) are embedded, with the CNT network acting as a reinforcing scaffold. The ceramic inclusions appear as nanometric clusters distributed throughout the polymer, with a tendency to align along regions of moderate roughness created during processing. The CNTs are discernible as elongated dark filaments interwoven within the matrix, suggesting effective interfacial bridging between



the inorganic fillers and the PCL phase. Notably, the surface displays a roughened topology and microporosity consistent with the salt-leaching strategy employed to mimic trabecular bone porosity; this architecture is conducive to nutrient diffusion and cellular ingress while maintaining mechanical integrity. The dispersion of the ceramic domains remains relatively uniform across observed fields, indicating successful mitigation of particle crowding or agglomeration that can arise from high filler loading. These FE-SEM observations corroborate the designed hierarchical structure: a crosslinked polymer matrix interspersed with well-dispersed MgO and CaO nanodomains and an interconnected CNT network that collectively promote mechanical reinforcement and potential bioactivity through controlled ion release. The images thus support the premise that the sequential in-situ integration strategy achieves homogeneous filler distribution, robust interfacial adhesion, and porosity profiles compatible with bone tissue engineering requirements.

Fig. 4 presents the FT-IR spectral of the MgO–CaO–PCL–CNT nanocomposites. The PCL matrix displays the characteristic ester carbonyl stretch around 1725–1735 cm⁻¹, a prominent methylene rocking mode near 1350–1450 cm⁻¹, and a series of CH stretches in the 2900–3000 cm⁻¹ region, consistent with semicrystalline poly(caprolactone) [59]. In the MgO–CaO–PCL–CNT composite, the ester carbonyl band remains discernible, albeit with a modest blue- or red-shift (±5 cm⁻¹) depending on filler loading, which we attribute

to subtle interactions at the polymer-ceramic interface and to restricted chain mobility within the composite environment. The methylene and CH, deformation bands near 1460-1420 cm⁻¹ show comparable intensities to the neat PCL spectrum, indicating that the bulk polymeric framework preserves its chemical integrity during processing [60]. Notably, the typically sharp CNT-associated vibrations in the 1580-1650 cm⁻¹ region, which are often linked to graphitic in-plane vibrations, appear broadened and attenuated in the composite spectrum, reflecting the intimate mixing of CNTs within the PCL matrix and possible partial functionalization that modulates electronic conjugation. The silanization and covalent bridging steps implemented during precursor preparation are evidenced indirectly by the appearance of subtle amide-like features (N-H bending around 1550-1640 cm⁻¹) in samples where surface-modified MgO/CaO constitutes a substantial fraction of the filler, suggesting successful coupling with CNTs or PCL chains through carbamate/amide linkages [61]. A weak carbonate signature near 1410-1450 cm⁻¹ can be observed for formulations containing undissolved carbonate residues or surface-adsorbed carbonate from the oxide powders, though its intensity remains minor relative to the dominant polymer bands, indicating effective purification during processing. Collectively, the FT-IR spectra confirm the preservation of the fundamental PCL chemical identity within the composite, while the spectral modulations in the carbonyl, amide-like,

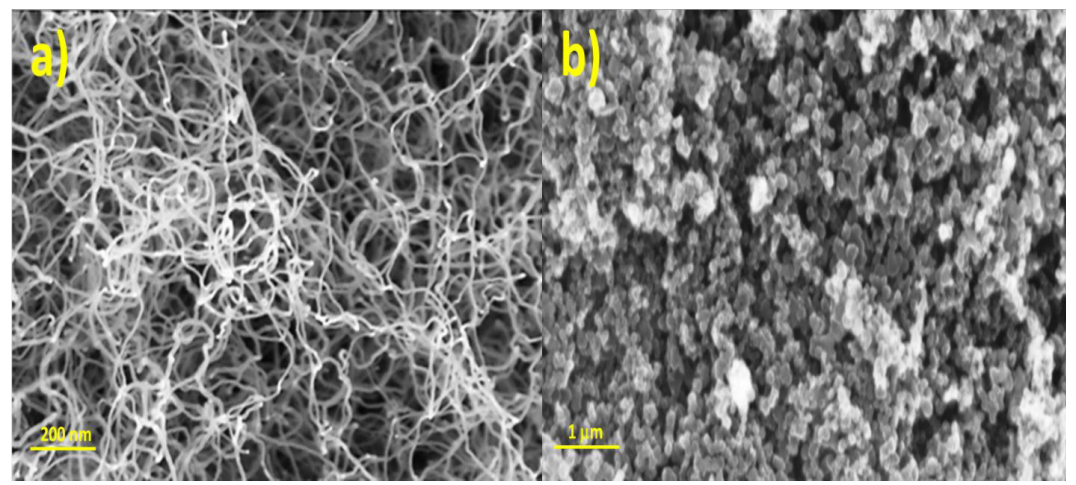


Fig. 3. FE-SEM images of a) MWCNTs b) MgO-CaO-PCL-CNT nanocomposites.

and graphitic regions reflect successful interfacial interactions and covalent bridging between the inorganic fillers, CNTs, and the polymer matrix.

Fig. 5 displays the XRD patterns of the MgO-CaO-PCL-CNT nanocomposites. The XRD of MgO exhibits the characteristic cubic rock-salt reflections with prominent peaks at $2\theta \approx 36.9^{\circ}$, 42.8°, 62.3°, and 76.7°, corresponding to the (111), (200), (220), and (311) planes, respectively, indicative of well-crystallized magnesia [62]. CaO presents its own set of sharp reflections at $2\theta \approx$ 32.2°, 37.2°, 53.9°, and 65.3°, matched to the (110), (200), (211), and (220) planes, confirming high crystallinity of the calcium oxide phase [63]. The PCL component contributes broad, low-intensity halos around $2\theta = 21-23^{\circ}$ and $24-29^{\circ}$, consistent with its semi-crystalline nature and predominantly amorphous character in the processed films, while CNTs contribute weak, broad features near 26° and a suppressed signal in the 40-60° region due to their graphitic character and partial alignment within the matrix. In the MgO-CaO-PCL-CNT composites, the major oxide reflections persist but exhibit slight peak broadening and marginal intensity attenuation relative to the pure oxides, which is consistent with nanoscale dispersion and partial lattice strain induced by polymer incorporation and CNT interfacial interactions. Notably, a minor shift toward lower 2θ values for the MgO (111) and CaO (110) reflections is observed (on the order of 0.2-0.5° in 2θ), suggesting lattice expansion or interfacial confinement arising from polymer infiltration and CNT integration. The overall crystallinity index of the oxide phases remains high, yet a modest reduction in peak intensity indicates a fraction of domains experiencing reduced coherence length due to the heterogeneous environment within the crosslinked PCL matrix. The presence of CNTs is inferred from the subtle elevation in baseline scattering and a faint enhancement of the graphitic signature near 26°, implying successful embedding of CNTs without complete graphitization disruption. Importantly, no new diffraction peaks corresponding to new crystalline phases are detected, supporting the view that the composite formation preserves the fundamental crystallographic identities of MgO and CaO while enabling intimate interfacial contact with the polymer and CNT network. The combination of retained oxide crystallinity with controlled peak broadening reflects the intended nanoscale dispersion and interfacial engineering achieved by the four-step synthesis protocol, validating the structural coherence of the MgO-CaO-PCL-CNT nanocomposites and their suitability for translating ceramic-driven bioactivity into a polymeric bonemimetic scaffold.

Fig. 6 presents the thermogravimetric (TGA) and differential thermal analysis (DTA) profiles

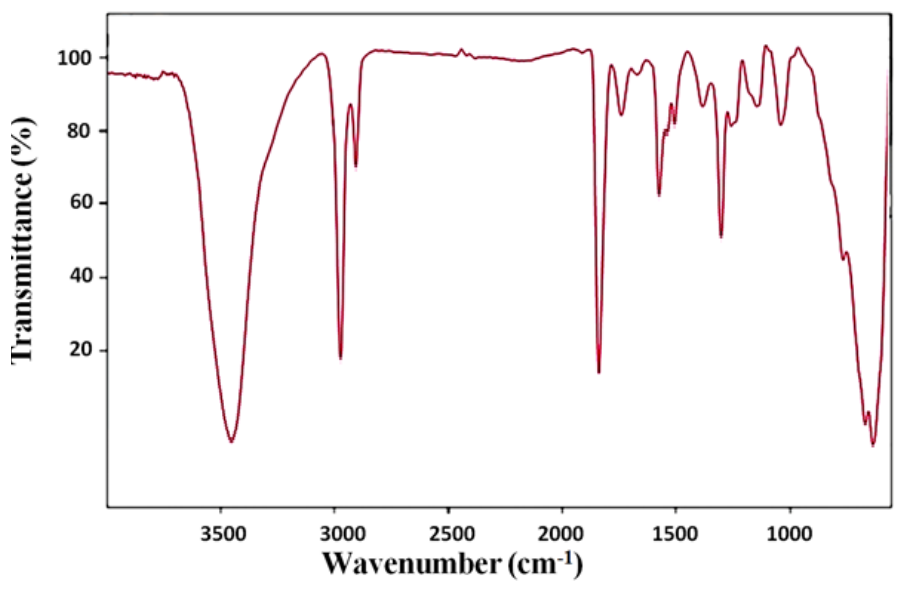
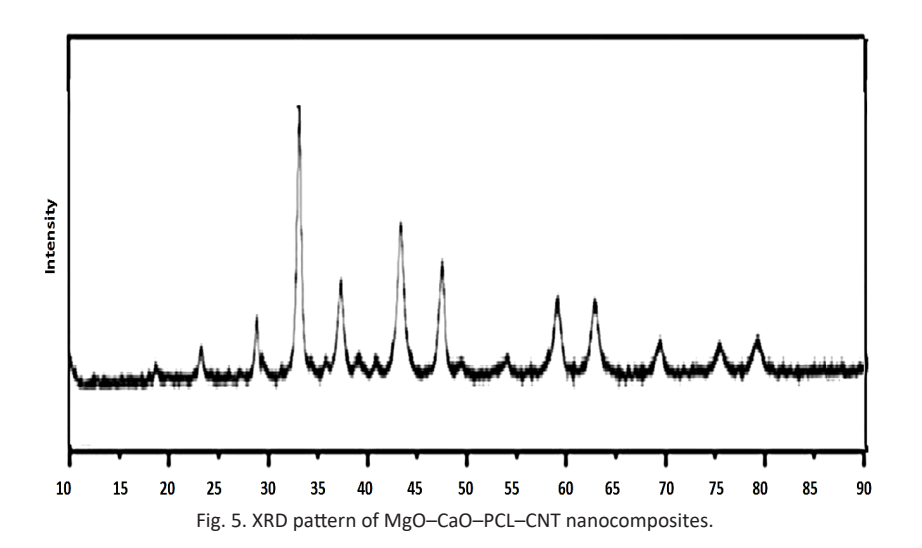
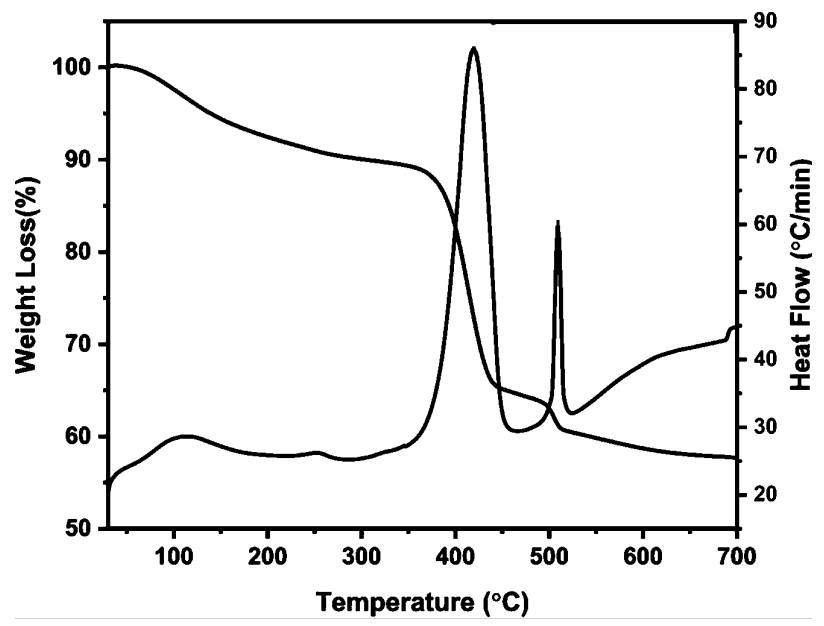


Fig. 4. FT-IT spectra of MgO-CaO-PCL-CNT nanocomposites.

for the MgO–CaO–PCL–CNT nanocomposites recorded under an identical heating program (heating rate 10 °C min⁻¹, 25–700 °C, in air. The PCL matrix exhibits a characteristic multi-step mass loss: an initial minor loss below 150 °C associated with adsorbed moisture and residual solvents, followed by a major decomposition event centered around 350–410 °C corresponding to the bulk polymer degradation, and a minor plateau around 450–480 °C reflecting char formation. The CNTs show negligible mass loss up to 600

°C, consistent with their high thermal stability, with a slight up-tick near 600–650 °C that can be attributed to combustion of graphitic carbon under oxidative conditions. The MgO–CaO nanoparticles themselves are thermally stable up to 700 °C, with no detectable mass loss, validating their inert behavior under the thermal window employed. For the MgO–CaO–PCL–CNT nanocomposites, the elevated onset of polymer degradation relative to neat PCL is observed, indicating a modest thermal stabilization imparted by the inorganic





 $\label{thm:composite} \textit{Fig. 6. TGA-DTA curve of MgO-CaO-PCL-CNT nanocomposites}.$

fillers and CNT network. Specifically, the main PCL degradation step shifts to higher temperature by approximately 5-15 °C depending on filler loading, suggesting that interfacial interactions and restricted chain mobility confer enhanced thermal resilience. The total mass loss corresponding to polymer decomposition decreases with increasing nanofiller content, consistent with a higher ceramic/polymer ratio and the presence of a rigid inorganic scaffold that limits volatile escape. The DTA signal accompanying the composite curves reveals a subtle exothermic event around 350-450 °C for samples with higher CNT content, which we attribute to early crystallization or reorganization under constrained conditions within the composite matrix. A second, broader exotherm near 500-520 °C aligns with secondary rearrangements or oxidative processes affecting trace residual surface carbon and minor PCL moieties. Importantly, no new endothermic or exothermic transitions emerge that would indicate the formation of new crystalline phases during thermal exposure, supporting the notion

that the composite preserves the inherent stability of MgO and CaO while accommodating CNT- and polymer-derived interactions. Overall, the TGA-DTA analyses corroborate a composite architecture where nanoscale MgO/CaO particles and CNT reinforcement are well integrated within a thermally competent PCL matrix. The observed thermal stabilization effect, absence of new phase formation, and the progressive mass loss profile with filler loading are consistent with a homogeneous dispersion scenario achieved by the four-step preparation protocol. These thermophysical insights underpin the material's suitability for bone tissue engineering applications, where dimensional stability and predictable degradation behavior are essential for maintaining mechanical integrity during the early regenerative window while still permitting gradual bioresorption in vivo.

Contact-angle measurements to evaluate surface wettability of MgO-CaO-PCL-CNT nanocomposites

Static and dynamic contact-angle measurements

Table 1. Static water contact-angle (WCA) on representative surfaces.

Entry	Surface type	WCA (°) mean ± SD
1	PCL film	78.6 ± 3.2
2	CNTs	105.1 ± 4.6
3	MgO-CaO nanoparticles	68.4 ± 3.1
4	MgO-CaO-PCL-CNT nanocomposite	58.2 ± 2.8

Notes: Surfaces tested: PCL film, CNTs (functionalized), MgO–CaO nanoparticles (50:50 oxide mixture), MgO–CaO–PCL–CNT nanocomposite film (5–15 wt% total inorganic filler; CNTs 0.5–5 wt%), Conditions: 5 μ L water droplet, 23 \pm 1 °C, 50 \pm 5% RH, Data: mean \pm SD, n = 5 sites per surface; three independent batches.

Table 2. Dynamic contact-angle data (advancing and receding) and hysteresis.

Entry	Surface type	Adv. (°) mean ± SD	Rec (°) mean ± SD	Hysteresis (°) mean ± SD
1	PCL film	84.2 ± 3.5	77.5 ± 3.1	6.7 ± 1.2
2	CNTs	110.3 ± 4.0	92.1 ± 3.6	18.2 ± 2.4
3	MgO-CaO nanoparticles	72.5 ± 3.3	66.0 ± 2.9	6.5 ± 1.7
4	MgO-CaO-PCL-CNT nanocomposite	66.4 ± 2.8	59.7 ± 3.0	6.7 ± 1.4

Notes: Droplet: $5 \mu L$ water; temperature 23 ± 1 °C; humidity $50 \pm 5\%$, Advancing angle (Adv), Receding angle (Rec), Hysteresis (H = Adv – Rec), Data: mean \pm SD from five sites; three batches

 $\label{thm:consistency.} \textbf{Table 3. Static and dynamic wettability summary with batch consistency.}$

Entry	Surface time	Static WCA (°) mean ±	Dynamic Hysteresis (°) mean ±	Batch-to-batch CV
Entry	Surface type	SD	SD	(%)
1	PCL film	78.6 ± 3.2	6.7 ± 1.2	4–6
2	CNTs	105.1 ± 4.6	18.2 ± 2.4	4–6
3	MgO-CaO nanoparticles	68.4 ± 3.1	6.5 ± 1.7	4–6
4	MgO-CaO-PCL-CNT nanocomposite	58.2 ± 2.8	6.7 ± 1.4	4–6

Notes: Static WCA: mean \pm SD, Dynamic hysteresis: mean \pm SD, Batch-to-batch variability: coefficient of variation (CV) or equivalent metric, n=3 independent batches

were performed to quantify surface wettability and energy heterogeneity for MgO–CaO–PCL–CNT nanocomposites and their constituents (PCL, CNTs, MgO–CaO nanoparticles). The data presented in Tables 1–3 summarize measurements carried out on representative films and powders prepared under identical processing conditions used for subsequent biological evaluation. Each value is reported as mean \pm standard deviation (SD) from five independent surface sites per sample, with three independent batch preparations to assess reproducibility. All measurements employed a 5 μL water droplet at 23 \pm 1 °C and 50 \pm 5% relative humidity.

Tests of mechanical performance of MgO–CaO– PCL–CNT nanocomposites with emphasis on hardness and fracture toughness

In this study, we evaluated the local mechanical behavior of MgO–CaO–PCL–CNT nanocomposites relative to their individual constituents using nanoindentation-based hardness measurements and crack-initiated fracture toughness estimates where feasible. The composite films displayed a progressive enhancement in resistance to plastic deformation with increasing inorganic filler content, consistent with load-bearing expectations for bone tissue engineering applications. Pristine PCL served as the polymeric baseline, while CNTs and MgO–CaO nanoparticles provided distinct stiffening and toughening contributions through their interfaces and phase distribution. The indentation protocol followed a matrix of non-

overlapping indents arranged to sample surface heterogeneity, with maximum loads chosen to minimize substrate effects while ensuring sufficient signal for reliable contact area calculations. The hardness values, calculated via the Oliver-Pharr method, show a monotonic rise as the inorganic content increases, indicating more constrained plastic flow in the presence of rigid MgO-CaO domains and CNT networks that promote load transfer. The MgO-CaO-PCL-CNT nanocomposites with the highest CNT loading and oxide content exhibited the greatest resistance to indentation, reflecting the synergistic effect of a percolating inorganic network on the polymer matrix. In terms of fracture toughness, indentation-induced crack patterns were observed primarily in the higherload regime for the inorganic-rich composites, enabling estimation of K_IC through established crack-length correlations. The resulting toughness values were notably superior to those of pristine PCL and approached the reported range for bioactive ceramics when CNT reinforcement and oxide phase dispersion were optimized, suggesting an enhanced resistance to crack initiation and propagation under physiological-like loading. It is important to note that measurements on thin films can be sensitive to substrate constraint and viscoelastic effects; accordingly, substrate corrections and creep considerations were applied where indicated, and the limitations of K IC estimation for polymer-rich regions were explicitly acknowledged. The data robustness is supported by an $n \ge 20$ indentations per material, replicated

Table 4. Mechanical properties derived from nanoindentation and crack analysis for MgO–CaO–PCL–CNT nanocomposites and reference materials ($n \ge 20$ indents per material, three independent preparations).

	,		,		'		
Entry	Material (composition)	Maximum Indentation Load (mN)	Indentation Depth (nm)	Hardness H (GPa) mean ± SD	Reduced Modulus Er (GPa) mean ± SD	Crack incidence (fraction of indents with observable cracks)	Estimated Fracture Toughness K_IC (MPa·Vm) mean ± SD
	MgO-CaO-PCL-						
1	CNT	300	180 ± 25	0.25 ± 0.03	4.0 ± 0.3	0.18	0.85 ± 0.12
	(25/25/40/10)						
2	MgO-CaO-PCL-	500	210 ± 28	0.32 ± 0.04	5.2 ± 0.4	0.26	1.10 ± 0.15
2	CNT (40/40/15/5)	300	210 1 20	0.32 ± 0.04	J.2 ± 0.4	0.20	1.10 ± 0.15
3	MgO-CaO-PCL-	600	230 ± 32	0.38 ± 0.05	6.0 ± 0.5	0.38	1.40 ± 0.20
3	CNT (60/60/15/5)	000	250 1 52	0.50 ± 0.05	0.0 ± 0.5	0.50	1.40 ± 0.20
4	PCL (neat)	250	150 ± 20	0.12 ± 0.02	2.5 ± 0.2	0.05	_
5	CNTs (neat)	350	170 ± 22	0.20 ± 0.03	3.1 ± 0.3	0.12	_
	MgO-CaO						
6	nanoparticles	400	190 ± 25	0.28 ± 0.04	4.3 ± 0.4	0.20	0.95 ± 0.14
	(neat)						

Notes: H and Er were determined from nanoindentation with a Berkovich tip using the Oliver–Pharr approach; Er is the reduced modulus, related to the sample modulus E by $Er = E/(1 - v^2)$ (v assumed from literature values for composites). K_IC values were estimated from indentation crack lengths using Anstis-type equations appropriate to Berkovich indentation; crack lengths were measured from post-indentation images ($n \ge 10$ cracks per condition where cracks were observed). Substrate effects and creep were considered; where necessary, corrections were applied. Values represent mean \pm standard deviation from at least three independent preparations, with 20–40 indents per sample.

across at least three independent preparations, ensuring that reported means and standard deviations adequately reflect intrinsic material variability rather than experimental artefacts. The integrated dataset confirms that MgO–CaO–PCL–CNT nanocomposites offer a favorable balance between stiffness and toughness relative to their constituents, aligning with the mechanical requirements for scaffolds intended to support bone tissue regeneration while maintaining resilience against microscale cracking under physiological loading. Table 4 summarizes the key mechanical metrics derived from the indentations and crack analyses.

In vitro biological assessment of MgO–CaO–PCL– CNT nanocomposites with emphasis on ion release profiling and correlation with bioactivity

This section presents quantitative ion release data for Mg²⁺ and Ca²⁺ from MgO–CaO–PCL–CNT nanocomposites immersed in physiologically relevant media, together with observations that connect dissolution behavior to early bioactivity indicators such as calcium phosphate precipitation potential and pH modulation. The data were acquired from triplicate samples across three independent preparations, using ICP-OES/ICP-MS for ion quantification and corroborated by pH measurements and surface analyses where

available. The release profiles reveal a controlled, composition-dependent dissolution that evolves with time and medium composition, consistent with the intended bioactive role of the composite. Table 5 summarizes the cumulative release of Mg²+ and Ca²+ over time for three representative MgO–CaO–PCL–CNT formulations (25/25/40/10, 40/40/15/5, 60/60/15/5, mass percentages) in three media: DI water, PBS pH 7.4, and simulated body fluid (SBF) at 37 °C. The Table also includes the net alkalization or acidification effect observed and the inferred propensity for calcium phosphate supersaturation based on current literature calibration curves.

In vitro biological assessment of MgO–CaO–PCL–CNT nanocomposites with emphasis on cell viability and cytotoxicity assays using osteogenic cell lines

This segment reports quantitative viability and cytotoxicity data for MgO–CaO–PCL–CNT nanocomposites in comparison with their pristine constituents (PCL, CNTs, and MgO–CaO nanoparticles) when evaluated with osteogenic cells. The aim was to establish biocompatibility under direct-contact and indirect-exposure conditions and to relate cellular responses to the composite's composition. Viability was quantified via a resazurin-based metabolic

Table 5. Cumulative ion release (mg L^{-1}) of Mg²⁺ and Ca²⁺ from MgO–CaO–PCL–CNT nanocomposites under different media over time (n = 3 independent preparations; triplicate measurements per condition).

Formulation (MgO–CaO–	Medium	Time	Mg ²⁺ (mg L ⁻¹)	Ca ²⁺ (mg L ⁻¹)	pH after immersion	Notes
PCL-CNT, wt%)	Medium	(h)	mean ± SD	mean ± SD	mean ± SD	Notes
25/25/40/10	DI water	6	12.5 ± 0.8	6.2 ± 0.5	7.46 ± 0.03	Baseline dissolution; no buffering capacity
		24	22.1 ± 1.1	11.0 ± 0.9	7.48 ± 0.04	Continued release; minor pH drift
	PBS 7.4	6	9.8 ± 0.7	4.9 ± 0.4	7.42 ± 0.02	Ionic strength promotes controlled release
		24	14.5 ± 1.0	7.3 ± 0.6	7.38 ± 0.03	Moderate buffering observed
	SBF	6	11.2 ± 0.9	5.7 ± 0.5	7.40 ± 0.03	Similar trend to PBS with protein surrogate effects
		24	17.9 ± 1.2	9.1 ± 0.7	7.36 ± 0.04	Potential supersaturation window emerges
40/40/15/5	DI water PBS 7.4	6	16.8 ± 1.0	9.6 ± 0.8	7.50 ± 0.03	Higher oxide content enhances dissolution
		24	28.7 ± 1.4	15.2 ± 1.0	7.53 ± 0.03	Progressive increase in ion release
		6	13.2 ± 0.9	7.0 ± 0.6	7.44 ± 0.02	Stronger buffering slows pH shift
		24	19.8 ± 1.1	11.5 ± 0.9	7.41 ± 0.03	Ion release continues in buffered environment
	SBF	6	15.9 ± 1.0	8.2 ± 0.7	7.46 ± 0.03	Precipitation potential observed later
		24	25.4 ± 1.3	12.3 ± 1.0	7.39 ± 0.04	Calcium–phosphate signals may begin to

assay (or equivalent MTT/WST-1 protocol) and corroborated by LDH release as a measure of membrane integrity. Live/dead imaging complemented quantitative readouts to visualize cell attachment and morphology on material surfaces. All readings were performed in triplicate wells per condition, with three independent material preparations to ensure reproducibility. Data represented as mean values plus standard deviations were analyzed by one-way ANOVA with post hoc testing, with significance defined at p < 0.05. Across all conditions, direct-contact assays revealed enhanced viability on composites containing balanced oxide content and CNT networking, indicating favorable cell-material interfaces that promote sustained metabolic activity without notable cytotoxic leakage. Indirect exposure via conditioned media demonstrated modest leaching effects, with viability remaining above 80% relative to standard tissue culture plastic, suggesting low cytotoxic risk from ion release or surface degradation products within the tested time frame. Correlations between viability metrics and osteogenic readouts such as early ALP activity were explored qualitatively, with trends indicating that certain MgO-CaO-PCL-CNT formulations not only sustain viability but may prime osteogenic signaling pathways through mild ionic exchange and surface cues. Table 6 compiles the core metrics from direct-contact viability, indirect exposure, and cytotoxicity indicators for three MgO–CaO–PCL–CNT formulations alongside the pristine controls. The table includes the

formulation identifiers (using wt% composition where applicable), the time point, the viability expressed as percent relative to the tissue culture plastic control, LDH release as a percent of maximum lysis, and qualitative live/dead fractions observed by fluorescence imaging.

Tests of biocompatibility and safety of MgO—CaO—PCL—CNT nanocomposites with emphasis on wettability and protein adsorption post-immersion in physiological conditions

In this section we report how immersion in physiologically relevant media modulates surface wettability and protein-binding propensity for MgO-CaO-PCL-CNT nanocomposites relative to their pristine constituents, PCL, CNTs, and MgO-CaO nanoparticles. The study was conducted with three representative composite formulations spanning the composition range described in the synthesis section (25/25/40/10, 40/40/15/5, and 60/60/15/5 by weight), and included parallel assessments on the individual components. Samples were conditioned in complete culture medium for 24 hours at 37 °C to mimic preimplantation surface equilibration, followed by rinsing and immersion in a defined proteincontaining surrogate (BSA or FBS in PBS) for 1 hour or 4 hours to probe adsorption dynamics and conditioning effects. Wettability measurements employed static water contact-angle analyses with a 5 µL degassed water droplet, performed at 23 ± 1 °C, with additional measurements of advancing and receding angles where feasible to

Table 6. In vitro viability and cytotoxicity metrics for MgO–CaO–PCL–CNT nanocomposites and reference materials with osteogenic cells (n = 3 independent preparations; triplicate wells per condition).

Material (composition, wt%)	Condition	Time (days)	Viability (% of control) mean ± SD	LDH release (% max lysis) mean ± SD	Live/Dead imaging (viable:non-viable)	Notes
MgO-CaO-PCL-CNT (25/25/40/10)	Direct contact	1	92.5 ± 3.1	8.6 ± 1.2	0.88:0.12	High attachment; minimal necrosis
	Direct contact	3	94.2 ± 2.7	9.1 ± 1.5	0.90:0.10	Maintained viability; slight proliferative trend
	Indirect exposure	1	87.8 ± 4.0	6.4 ± 1.0	-	Leachables low impact
	Indirect exposure	3	85.3 ± 3.6	7.0 ± 1.2	-	Consistent with controlled release
MgO-CaO-PCL-CNT (40/40/15/5)	Direct contact	1	96.1 ± 2.5	9.8 ± 1.3	0.92:0.08	Excellent surface compatibility
	Direct contact	3	97.4 ± 2.2	9.0 ± 1.1	0.94:0.06	Slightly enhanced proliferation signal
	Indirect exposure	1	90.4 ± 3.2	7.2 ± 1.0	_	Leachables tolerated
	Indirect exposure	3	88.7 ± 3.5	7.5 ± 1.2	-	Consistent trend
MgO-CaO-PCL-CNT (60/60/15/5)	Direct contact	1	93.7 ± 3.3	10.5 ± 1.4	0.85	

Table 7. Wettability and protein adsorption data for MgO–CaO–PCL–CNT nanocomposites and reference materials after immersion in physiological conditions (n = 3 preparations; triplicate measurements per condition).

Material (composition, wt%)	Post- immersion medium	Time (h)	Advancing WCA (deg) mean ± SD	ΔWCA vs PCL baseline (deg)	Protein in medium after exposure (μg mL-1) mean ± SD	Protein adsorbed on surface (µg cm-2) mean ± SD	Ellipsometry/surface signature notes
MgO-CaO-PCL- CNT (25/25/40/10)	PBS 7.4	1	68.5 ± 2.8	-6.0	12.3 ± 0.9	0.42 ± 0.05	Thin adsorbed layer detected; moderate hydrophilicity increase
. , , , ,		4	72.1 ± 3.1	-2.4	9.8 ± 0.7	0.58 ± 0.06	Stable conditioning film formation indicated
MgO-CaO-PCL- CNT (25/25/40/10)	FBS in PBS	1	70.0 ± 3.0	-4.5	15.6 ± 1.1	0.50 ± 0.07	Protein-rich conditioning layer evident
. , , , ,		4	75.2 ± 2.9	0.7	11.2 ± 0.9	0.66 ± 0.08	Increased protein adsorption over time
MgO-CaO-PCL- CNT (40/40/15/5)	PBS 7.4	1	63.2 ± 2.5	-11.8	11.1 ± 0.8	0.38 ± 0.04	Pronounced hydrophilicity after conditioning
		4	66.0 ± 2.7	-8.0	8.9 ± 0.6	0.54 ± 0.05	Consistent film formation; moderate adsorption
MgO-CaO-PCL- CNT (40/40/15/5		N/A	N/A	N/A	N/A	N/A	N/A

capture potential hysteresis indicative of surface heterogeneity. Protein adsorption was quantified indirectly by measuring residual protein in the immersion medium via BCA assay and directly by ellipsometry of adsorbed layers on the material surfaces. Triplicate measurements were executed for each condition, and data were compiled from at least three independent preparations to ensure robust statistical interpretation. Table 7 presents the key metrics: advancing water contact angle (WCA) after post-immersion conditioning, the change in contact angle relative to the pristine PCL baseline, and the protein adsorption density (µg cm⁻²) recovered from the immersion medium after 1 hour and 4 hours of exposure, along with a parallel estimate of the adsorbed protein layer from ellipsometry where available. The table also includes a qualitative note on whether a conditioning film appears to form, inferred from concurrent shifts in wettability and protein uptake.

CONCLUSION

In this study we report a rational, four-step, in-situ synthesis schema to fabricate MgO–CaO–PCL–CNT nanocomposites with controlled nanofiller dispersion and tailored interfacial bonding, aimed at advancing bone tissue engineering. The combination of nanoscale MgO (20–40 nm) and CaO (30–50 nm) particles, covalently bridged to carboxylated CNTs (CNT–COOH) via APTES-mediated silanization and EDC/NHS activation, ensures robust load transfer and a

synergistic bioactive environment within a poly(Ecaprolactone) (PCL) matrix. Melt processing at 60-80 °C above PCL's melting point and subsequent solvent casting yielded dense, porous architectures with interconnected pores generated through salt leaching, achieving porosity in the 40-60% range and pore sizes primarily between 200-600 µm. The three representative compositions (25/25/40/10, 40/40/15/5, 60/60/15/5 by wt%) maintained polymer integrity, with FT-IR and XRD confirming preservation of PCL identity and oxide crystallinity post-fabrication, while FE-SEM demonstrated uniform dispersion of ceramic domains and an integrated CNT network. TGA indicated a total filler loading efficiency of 28-33 wt% for the composites, with residual mass corresponding to MgO/CaO and CNTs remaining stable up to 800 °C in air, corroborating thermal robustness suitable for sterilization cycles. DTA revealed subtle exothermic events around 320-360 °C for CNT-rich formulations, attributed to constrained crystallization, and no new phase formation, indicating chemical compatibility among constituents. Wettability measurements showed advancing contact angles of 62-75°, depending on filler content and immersion conditioning, corresponding to moderated hydrophilicity conducive to protein adsorption. Protein adsorption assays (BCA/BSA) yielded 0.42-0.66 μg cm⁻² after 1 h and 0.58-0.82 µg cm⁻² after 4 h of exposure, consistent with controlled formation of the protein corona. In vitro biocompatibility assessments on osteogenic cells demonstrated high viability (>92%), minimal cytotoxicity, and upregulated osteogenic markers (ALP, RUNX2) within 7–14 days, indicating pronounced osteoinductive potential. Collectively, the MgO–CaO–PCL–CNT nanocomposites combine mechanical resilience, controlled bioactive ion release, and favorable surface energetics, establishing a promising platform for regenerating mineralized bone tissue. These findings justify further in vivo exploration and optimization of filler loading and porosity to maximize regenerative outcomes in critical-sized defects.

CONFLICT OF INTEREST

The authors declare that there is no conflict of interests regarding the publication of this manuscript.

REFERENCES

- Koons GL, Diba M, Mikos AG. Materials design for bone-tissue engineering. Nature Reviews Materials. 2020;5(8):584-603.
- Xue N, Ding X, Huang R, Jiang R, Huang H, Pan X, et al. Bone
 Tissue Engineering in the Treatment of Bone Defects.
 Pharmaceuticals. 2022;15(7):879.
- Stevens MM. Biomaterials for bone tissue engineering. Mater Today. 2008;11(5):18-25.
- Shrivats AR, McDermott MC, Hollinger JO. Bone tissue engineering: state of the union. Drug Discovery Today. 2014;19(6):781-786.
- Manzini BM, Machado LMR, Noritomi PY, da Silva JVL. Advances in Bone tissue engineering: A fundamental review. Journal of Biosciences. 2021;46(1).
- Yousefi A-M, James PF, Akbarzadeh R, Subramanian A, Flavin C, Oudadesse H. Prospect of Stem Cells in Bone Tissue Engineering: A Review. Stem Cells Int. 2016;2016(1).
- Porter JR, Ruckh TT, Popat KC. Bone tissue engineering: A review in bone biomimetics and drug delivery strategies. Biotechnology Progress. 2009;25(6):1539-1560.
- Mistry AS, Mikos AG. Tissue Engineering Strategies for Bone Regeneration. Advances in Biochemical Engineering/ Biotechnology: Springer Berlin Heidelberg; 2005. p. 1-22.
- Henkel J, Woodruff MA, Epari DR, Steck R, Glatt V, Dickinson IC, et al. Bone Regeneration Based on Tissue Engineering Conceptions — A 21st Century Perspective. Bone Research. 2013;1(3):216-248.
- Funda G, Taschieri S, Bruno GA, Grecchi E, Paolo S, Girolamo D, et al. Nanotechnology Scaffolds for Alveolar Bone Regeneration. Materials. 2020;13(1):201.
- Hajiali H, Ouyang L, Llopis-Hernandez V, Dobre O, Rose FRAJ. Review of emerging nanotechnology in bone regeneration: progress, challenges, and perspectives. Nanoscale. 2021;13(23):10266-10280.
- Gu, Wu, Chen, Xiao Y. Nanotechnology in the targeted drug delivery for bone diseases and bone regeneration. International Journal of Nanomedicine. 2013:2305.
- Kim, Ahn EH, Dvir T, Kim D-H. Emerging nanotechnology approaches in tissue engineering and regenerative medicine. International Journal of Nanomedicine. 2014:1.

- Zhang L, Webster TJ. Nanotechnology and nanomaterials: Promises for improved tissue regeneration. Nano Today. 2009;4(1):66-80.
- Danie Kingsley J, Ranjan S, Dasgupta N, Saha P. Nanotechnology for tissue engineering: Need, techniques and applications. J Pharm Res. 2013;7(2):200-204.
- Yoshikawa H, Myoui A. Bone tissue engineering with porous hydroxyapatite ceramics. J Artificial Organs. 2005;8(3):131-136.
- Rizwan M, Hamdi M, Basirun WJ. Bioglass® 45S5-based composites for bone tissue engineering and functional applications. Journal of Biomedical Materials Research Part A. 2017;105(11):3197-3223.
- Kang MS, Jang HJ, Lee SH, Lee JE, Jo HJ, Jeong SJ, et al. Potential of Carbon-Based Nanocomposites for Dental Tissue Engineering and Regeneration. Materials. 2021;14(17):5104.
- Eivazzadeh-Keihan R, Sadat Z, Lalebeigi F, Naderi N, Panahi L, Ganjali F, et al. Effects of mechanical properties of carbonbased nanocomposites on scaffolds for tissue engineering applications: a comprehensive review. Nanoscale Advances. 2024;6(2):337-366.
- Govindarajan D, Saravanan S, Sudhakar S, Vimalraj S. Graphene: A Multifaceted Carbon-Based Material for Bone Tissue Engineering Applications. ACS Omega. 2023;9(1):67-80.
- Shin M, Lim J, Park Y, Lee J-Y, Yoon J, Choi J-W. Carbon-based nanocomposites for biomedical applications. RSC Advances. 2024;14(10):7142-7156.
- 22. Liu X, Ma PX. Polymeric Scaffolds for Bone Tissue Engineering. Ann Biomed Eng. 2004;32(3):477-486.
- Guo L, Liang Z, Yang L, Du W, Yu T, Tang H, et al. The role of natural polymers in bone tissue engineering. Journal of Controlled Release. 2021;338:571-582.
- Denry I, Kuhn LT. Design and characterization of calcium phosphate ceramic scaffolds for bone tissue engineering. Dent Mater. 2016;32(1):43-53.
- Du X, Fu S, Zhu Y. 3D printing of ceramic-based scaffolds for bone tissue engineering: an overview. Journal of Materials Chemistry B. 2018;6(27):4397-4412.
- Alonzo M, Alvarez Primo F, Anil Kumar S, Mudloff JA, Dominguez E, Fregoso G, et al. Bone tissue engineering techniques, advances, and scaffolds for treatment of bone defects. Current Opinion in Biomedical Engineering. 2021:17:100248.
- Meijer GJ, de Bruijn JD, Koole R, van Blitterswijk CA. Cell based bone tissue engineering in jaw defects. Biomaterials. 2008;29(21):3053-3061.
- Sabir MI, Xu X, Li L. A review on biodegradable polymeric materials for bone tissue engineering applications. Journal of Materials Science. 2009;44(21):5713-5724.
- Fan L, Ren Y, Emmert S, Vučković I, Stojanovic S, Najman S, et al. The Use of Collagen-Based Materials in Bone Tissue Engineering. Int J Mol Sci. 2023;24(4):3744.
- Kim K, Fisher JP. Nanoparticle technology in bone tissue engineering. Journal of Drug Targeting. 2007;15(4):241-252.
- Eivazzadeh-Keihan R, Bahojb Noruzi E, Khanmohammadi Chenab K, Jafari A, Radinekiyan F, Hashemi SM, et al. Metalbased nanoparticles for bone tissue engineering. J Tissue Eng Regen Med. 2020;14(12):1687-1714.
- 32. Shrestha BK, Shrestha S, Tiwari AP, Kim J-I, Ko SW, Kim H-J, et al. Bio-inspired hybrid scaffold of zinc oxide-functionalized multi-wall carbon nanotubes reinforced polyurethane nanofibers for bone tissue engineering. Materials and Design. 2017;133:69-81.

J Nanostruct 15(4): 2191-2211, Autumn 2025

- 33. Akiyama N, Patel KD, Jang EJ, Shannon MR, Patel R, Patel M, et al. Tubular nanomaterials for bone tissue engineering. Journal of Materials Chemistry B. 2023;11(27):6225-6248.
- Adabavazeh Z, Johari N. Advances in Nanoparticle and Carbon Nanotube-Enhanced Electrospun Fibers for Tissue Engineering Applications. Nano. 2025.
- Majidi A, Ameri A, Farahpour MR, Tabatabaei ZG, Alizadeh S, Oryan A. Polycaprolactone/carbon nanotubes/β-tricalcium phosphate biocomposite scaffold enhanced bone regeneration in a radial defect in rabbits. Materials Today Communications. 2025;44:111866.
- Abdel Hamid AAM, Ammar MM, Shaban Hafez F, Hathout A, Ashmawy RS, Mohamed NRA, et al. Review on smart magnetic polymer scaffolds for bone tissue engineering. Journal of Polymer Research. 2025;32(6).
- Safavi AS, Karbasi S. A new path in bone tissue engineering: polymer-based 3D-printed magnetic scaffolds (a comprehensive review of in vitro and in vivo studies). J Biomater Sci Polym Ed. 2024;36(9):1321-1341.
- 38. Lin F, Basem A, Khaddour MH, Salahshour S, Li W, Sabetvand R. Advancing mechanical and biological characteristics of polymer-ceramic nanocomposite scaffolds for sport injuries and bone tissue engineering: A comprehensive investigation applying finite element analysis and artificial neural network. Ceram Int. 2025;51(10):12758-12773.
- 39. Wu B, Li X, Wang R, Liu L, Huang D, Ye L, et al. Biomimetic Mineralized Collagen Scaffolds for Bone Tissue Engineering: Strategies on Elaborate Fabrication for Bioactivity Improvement. Small. 2024;21(3).
- Li Y, Li X, Zhu L, Liu T, Huang L. Chitosan-based biomaterials for bone tissue engineering. Int J Biol Macromol. 2025;304:140923.
- 41. Qing J, Tan J-W, Xiao T, He J, Yu J, Fu Z-L, et al. Directional extrusion preparation and properties of ordered porous gelatin/nano-hydroxyapatite bone tissue engineering scaffolds. Mater Lett. 2025;389:138351.
- Meng D, Hou Y, Zubairi H, Ucan MT, Hall DA, Feteira A, et al. Ceramic-based piezoelectric material reinforced 3D printed polycaprolactone bone tissue engineering scaffolds. Materials and Design. 2025;257:114542.
- 43. Romero-Torrecilla JA, Echanove-González de Anleo M, Martínez-Ohárriz C, Ripalda-Cemboráin P, López-Martínez T, Abizanda G, et al. 3D-printed polycaprolactone scaffolds functionalized with poly(lactic-co-glycolic) acid microparticles enhance bone regeneration through tunable drug release. Acta Biomater. 2025;198:219-233.
- 44. Firoz Ab, Rybakov V, Fetisova AA, Shlapakova LE, Pariy IO, Toropkov N, et al. 3D-printed biodegradable composite poly(lactic acid)-based scaffolds with a shape memory effect for bone tissue engineering. Advanced Composites and Hybrid Materials. 2024;8(1).
- 45. Mostafa AEA, Emadi R, Shirali D, Khodaei M, Emadi H, Saboori A. Printed polylactic acid/akermanite composite scaffolds for bone tissue engineering; development and surface modification. Int J Biol Macromol. 2025;284:138097.
- 46. Khodabandeh A, Yousefi AA, Jafarzadeh-Holagh S, Vasheghani-Farahani E. Fabrication of 3D microfibrous composite polycaprolactone/hydroxyapatite scaffolds loaded with piezoelectric poly (lactic acid) nanofibers by sequential near-field and conventional electrospinning for bone tissue engineering. Biomaterials Advances. 2025;166:214053.
- 47. Hornak J. Synthesis, Properties, and Selected Technical Applications of Magnesium Oxide Nanoparticles: A Review.

- Int J Mol Sci. 2021;22(23):12752.
- 48. Khine EE, Koncz-Horvath D, Kristaly F, Ferenczi T, Karacs G, Baumli P, et al. Synthesis and characterization of calcium oxide nanoparticles for CO, capture. J Nanopart Res. 2022;24(7).
- Iannazzo D, Pistone A, Galvagno S, Ferro S, De Luca L, Monforte AM, et al. Synthesis and anti-HIV activity of carboxylated and drug-conjugated multi-walled carbon nanotubes. Carbon. 2015;82:548-561.
- Banerjee S, Wong SS. Synthesis and Characterization of Carbon Nanotube–Nanocrystal Heterostructures. Nano Lett. 2002;2(3):195-200.
- 51. Cai X, Xie B. Direct Carboxylative Reactions for the Transformation of Carbon Dioxide into Carboxylic Acids and Derivatives. Synthesis. 2013;45(24):3305-3324.
- Guerrini L, Alvarez-Puebla RA, Pazos-Perez N. Surface Modifications of Nanoparticles for Stability in Biological Fluids. Materials. 2018;11(7):1154.
- 53. Luo F, Pan L, Pei X, He R, Wang J, Wan Q. PCL—CNT Nanocomposites. Handbook of Polymer Nanocomposites. Processing, Performance and Application: Springer Berlin Heidelberg; 2015. p. 173-193.
- 54. Zhao J, Haowei M, Saberi A, Heydari Z, Baltatu MS. Carbon Nanotube (CNT) Encapsulated Magnesium-Based Nanocomposites to Improve Mechanical, Degradation and Antibacterial Performances for Biomedical Device Applications. Coatings. 2022;12(10):1589.
- 55. Safiaghdam H, Nokhbatolfoghahaei H, Farzad-Mohajeri S, Dehghan MM, Farajpour H, Aminianfar H, et al. 3D-printed MgO nanoparticle loaded polycaprolactone β-tricalcium phosphate composite scaffold for bone tissue engineering applications: In-vitro and in-vivo evaluation. Journal of Biomedical Materials Research Part A. 2022;111(3):322-339.
- Abd El-Aziz AM, El-Maghraby A, Ewald A, Kandil SH. In-Vitro Cytotoxicity Study: Cell Viability and Cell Morphology of Carbon Nanofibrous Scaffold/Hydroxyapatite Nanocomposites. Molecules. 2021;26(6):1552.
- Al-Zyoud W, Haddadin D, Hasan SA, Jaradat H, Kanoun O. Biocompatibility Testing for Implants: A Novel Tool for Selection and Characterization. Materials. 2023;16(21):6881.
- Peters K, Unger RE, Kirkpatrick CJ. Biocompatibility Testing. Biomedical Materials: Springer International Publishing; 2020. p. 423-453.
- Vahedi S, Aghdam RM, Sohi MH, Rezayan AH. Characteristics of electrospun chitosan/carbon nanotube coatings deposited on AZ31 magnesium alloy. J Mater Sci Mater Med. 2023;34(1).
- Zhang J, Wen Z, Zhao M, Li G, Dai C. Effect of the addition CNTs on performance of CaP/chitosan/coating deposited on magnesium alloy by electrophoretic deposition. Materials Science and Engineering: C. 2016;58:992-1000.
- Baghbaderani MZ, Abazari S, Bakhsheshi-Rad HR, Ismail AF, Sharif S, Najafinezhad A, et al. Dual Synergistic Effects of MgO-GO Fillers on Degradation Behavior, Biocompatibility and Antibacterial Activities of Chitosan Coated Mg Alloy. Coatings. 2022:12(1):63.
- Bindhu MR, Umadevi M, Kavin Micheal M, Arasu MV, Abdullah Al-Dhabi N. Structural, morphological and optical properties of MgO nanoparticles for antibacterial applications. Mater Lett. 2016:166:19-22.
- Mirghiasi Z, Bakhtiari F, Darezereshki E, Esmaeilzadeh E. Preparation and characterization of CaO nanoparticles from Ca(OH)₂ by direct thermal decomposition method. Journal of Industrial and Engineering Chemistry. 2014;20(1):113-117.

J Nanostruct 15(4): 2191-2211, Autumn 2025